Check for updates

Characterization of encapsulated graphene layers using extreme ultraviolet coherence tomography

FELIX WIESNER,[1,2,7,8] (ID) SLAWOMIR SKRUSZEWICZ,[1,2,3,7,9] (ID)
CHRISTIAN RÖDEL,[4] JOHANN JAKOB ABEL,[1] JULIUS REINHARD,[1,2]
MARTIN WÜNSCHE,[1,2] JAN NATHANAEL,[1,2] MARCO GRÜNEWALD,[5]
UWE HÜBNER,[6] GERHARD G. PAULUS,[1,2] AND SILVIO FUCHS[1,2]

[1]*Institute of Optics and Quantum Electronics, Friedrich Schiller University Jena, Max-Wien-Platz 1, 07743 Jena, Germany*
[2]*Helmholtz Institute Jena, Fröbelstieg 3, 07743 Jena, Germany*
[3]*Deutsches Elektronen Synchrotron DESY, Notkestraße 85, 22607 Hamburg, Germany*
[4]*Institute of Nuclear Physics, TU Darmstadt, Schlossgartenstraße 9, 64289 Darmstadt, Germany*
[5]*Institute of Solid State Phyiscs, Friedrich Schiller University Jena, Max-Wien-Platz 1, 07743 Jena, Germany*
[6]*Leibniz Institute of Photonic Technology, Albert-Einstein-Straße 9, 07743 Jena, Germany*
[7]*These authors contributed equally to this work.*
[8]*felix.wiesner@uni-jena.de*
[9]*slawomir.skruszewicz@desy.de*

Abstract: Many applications of two-dimensional materials such as graphene require the encapsulation in bulk material. While a variety of methods exist for the structural and functional characterization of uncovered 2D materials, there is a need for methods that image encapsulated 2D materials as well as the surrounding matter. In this work, we use extreme ultraviolet coherence tomography to image graphene flakes buried beneath 200 nm of silicon. We show that we can identify mono-, bi-, and trilayers of graphene and quantify the thickness of the silicon bulk on top by measuring the depth-resolved reflectivity. Furthermore, we estimate the quality of the graphene interface by incorporating a model that includes the interface roughness. These results are verified by atomic force microscopy and prove that extreme ultraviolet coherence tomography is a suitable tool for imaging 2D materials embedded in bulk materials.

1. Introduction

Graphene is a novel allotrope of carbon consisting of only a single layer of atoms forming a 2D lattice. Since its demonstration in 2004 [1], it has enthralled researchers with a broad range of unique properties such as very high carrier mobility, the quantum Hall effect at room temperature, or ambipolar electric field effects along with ballistic conduction of charge carriers [2]. All of them make graphene a promising material that has found uses in many new applications, such as manufacturing efficient p-n junctions [3], supercapacitors [4], or ultra-sensitive biosensors [5]. Various microscopic and spectroscopic techniques have been applied to the characterization of graphene [6], aiming at the determination of the number of layers and the purity of the sample in terms of the presence of defects. The most versatile and extensively used diagnostic is based on Raman spectroscopy [7,8]. The Raman spectrum provides information on the number and orientation of layers, doping, and disorder of functional groups. Other methods are atomic force microscopy (AFM) [9], transmission electron microscopy (TEM) [10], high-resolution

scanning tunneling microscopy (STM) [11], X-ray diffraction (XRD), electron diffraction, optical microscopy [12,13], and time-of-flight secondary ion mass spectrometry (ToF-SIMS) [14]. For a comprehensive review of characterization methods see Ref. [15]. However, nearly all of these methods are used to investigate graphene that is deposited on top of the sample. Inspection of encapsulated graphene is strongly limited, for example by the transmission of the Raman lasers or the high-energy electron beam in TEM. Investigation of encapsulated graphene using ellipsometry is in principle possible, however, significant limitations and challenges remain to be solved [16]. Encapsulated graphene can be identified by optical contrast microscopy but only for defined thicknesses of the encapsulation [17].

Recently, extreme ultraviolet coherence tomography (XCT) has emerged as a highly sensitive cross-sectional imaging technique of thin layers [18–20]. To date, XCT is able to provide 3D tomographic images of a sample with nanometer-scale depth resolution and micrometer-scale lateral resolution [21]. It is a non-invasive and non-destructive technique based on the measurement of the broadband reflectivity in the extreme ultraviolet (EUV or XUV). Here we demonstrate that XCT can provide simultaneous localization and characterization of graphene in an encapsulating homogeneous matrix or a sophisticated three-dimensional structure. As graphene has to be buried under a protective capping layer for many applications, a characterization of encapsulated graphene with XCT could be important for developing efficient ultrathin optoelectronic devices, transistors, and sensors. We anticipate that the non-invasive imaging and characterization of buried graphene with XCT can become a complementary technique to, e.g., Raman spectroscopy.

We start by giving a brief review of the concepts of XCT relevant for the characterization of embedded two-dimensional materials. Next, we show results on the three-dimensional imaging of graphene encapsulated in silicon. Finally, we outline an approach to obtain the roughness of the graphene among other parameters by a model-based reconstruction of the sample's structure.

2. Methods

2.1. Extreme ultraviolet coherence tomography (XCT)

Graphene samples were investigated using a laser-based XCT setup which is described in detail in Ref. [21]. EUV radiation with a large bandwidth is generated by high-harmonic generation (HHG) [22] in argon driven by ~ 40-fs laser pulses from a three-stage optical parametric amplifier [23]. The EUV radiation is filtered with a 200-nm aluminum foil and has a bandwidth of $38 - 72$ eV. Subsequently, it is focused to a spot size of $\sim 50\,\mu$m on the sample with a toroidal mirror. The sample holder allows the positioning of samples in the EUV focus such that the lateral translation of the sample allows a 2D scan. The sample is placed at an incidence angle of $15°$ and reflects the EUV radiation to a highly sensitive EUV spectrometer [24].

The scheme of XCT is a variant of Fourier-domain common-path interferometry as illustrated in Fig. 1. Accordingly, the depth structure of the sample is retrieved from a broadband reflectivity measurement. For describing the principle of XCT, we assume that the multilayer sample consists of a surface with field reflectivity $r_S(\omega)$, and buried interfaces with reflectivities $r_j(\omega)$ located at depths z_j. With the broadband EUV light source, spectral modulations occur in the reflected spectrum due to the interference of light reflected at these interfaces. The field reflectivity of the sample can be written as

$$r(\omega) = r_S(\omega) + \sum_{j=1}^{N} r_j(\omega)e^{2ik_z(\omega)z_j} \tag{1}$$

with buried interfaces at a distance of z_j to the surface. Here, dispersion is approximated using the real part of the wave vector $k_z(\omega)$ in the dominant sample material [20]. Multiple reflections can be neglected due to the low reflectivity of interfaces in the EUV at the steep incidence angles used. The depth structure of the sample $r(z)$ is obtained from the Fourier transform of Eq. (1).
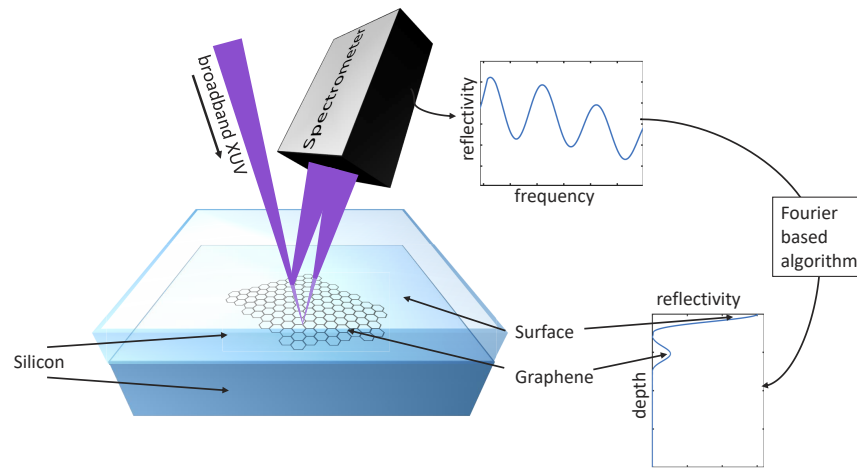
Fig. 1. Schematic of XCT of a buried graphene layer under a silicon capping layer: Broadband EUV radiation is focused on the sample. The EUV radiation is partially reflected from the surface and the graphene interface. Spectral interference of the partial waves causes a modulation of the reflected spectrum. The modulations contain the information of the depth structure, which can be obtained using a phase retrieval algorithm [19].

The temporal coherence length of the incident EUV radiation determines the depth resolution of XCT. Our broadband HHG source enables a theoretical depth resolution of

$$\delta_z \sim \lambda^2/\Delta\lambda = 27\,\text{nm} \quad , \tag{2}$$

where λ and $\Delta\lambda$ are the center wavelength and the bandwidth, respectively.

However, the field reflectivity $r(\omega)$ cannot be recorded directly with common detectors since the phase information is lost. We solve this problem with a one-dimensional iterative phase-retrieval algorithm [19]. The algorithm can reconstruct the phase information from the absolute value of the reflectivity $|r(\omega)|$ for each lateral point individually. It is capable of an unambiguous reconstruction of the sample's depth structure, or more precisely the depth-dependent reflectivity profile $r(z)$ of the sample [25].

It is important to note that the phase retrieval algorithm requires an accurate measurement of the reflectivity over a large bandwidth. This implies the necessity of a stable and well-characterized EUV source spectrum. Therefore, we determine the source spectrum by measuring the reflected spectrum of a reference sample with known reflectivity prior to the measurement of the actual sample.

A three-dimensional image of the sample can be obtained by laterally moving the sample under the EUV focus while recording the sample's reflectivity at each position. The XCT algorithm is then performed for each lateral position separately. Besides the structural information, the reconstructed complex reflectivity at every lateral point can be further investigated to determine the frequency-dependent reflectivity $r_S(\omega)$ and $r_j(\omega)$ and thus material information of all involved layers by using truncated Fourier transforms in the reconstruction [26].

2.2. Sample preparation

The graphene samples were manufactured by the commercial vendor Graphenea [27]. They grow graphene (approx. 4×4 mm) by chemical vapor deposition (CVD) on a copper substrate and transfer the 2D material onto a silicon substrate using polymethylmethacrylate (PMMA). The substrate has a nanometer-thin oxidation layer (SiO_2) on its surface. Different samples

were prepared with mono- (ML), bi- (BL), and trilayers (TL) of graphene. Since the growth of graphene monolayers is a self-limiting process, the BLs and TLs were produced by multiple transfers of monolayers on top of each other. After each transfer, the PMMA was removed using acetone. Three samples (one per ML,BL,TL) were then coated with a 200-nm capping layer of amorphous silicon using magnetron sputtering. These samples were processed simultaneously to ensure they were exposed to the same conditions during the deposition process. One sample of each type (ML, BL, TL) was left uncoated to allow comparative investigation with different methods.

3. Results

3.1. Three-dimensional imaging of encapsulated graphene

Three-dimensional tomograms of the three encapsulated samples (ML, BL, TL) were recorded with XCT as described in chapter 2.1. These tomograms are shown in the second column of Fig. 2. The normalized color scale encodes the depth-dependent phase-retrieved reflectivity $r(z)$ and thus shows the depth structure of the sample. Note that proportions in xy-plane and along the z-axis (depth) are different. In the experiment, the lateral resolution is about 250 μm due to the coarse scanning. The axial resolution is 27 nm, which corresponds to the temporal coherence length of the EUV spectrum (see Eq. (2)). Obviously, this resolution is much larger than the thickness of a graphene layer ($\Delta d = 0.335$ nm for a monolayer [28]). Nevertheless, the tomographic images clearly reveal interfaces at 200 nm beneath the capping layer. The good signal contrast is caused by the strong change in the refractive index at the graphene interface. In addition, the axial precision of the XCT measurement is significantly better than the axial resolution [19]. The rectangular shape of the graphene interfaces (4×4 mm) is clearly visible in the three-dimensional reconstruction of the sample. A weaker interface between the amorphous deposited silicon and the silicon substrate is also visible. This is due to a thin native oxide layer on the silicon substrate. The reconstruction of the tomograms and the measurement of the capping layer thickness are accomplished based on the XCT method described in section 2.1 and do not require additional modeling.

In addition, Fig. 2 shows images of the absolute reflectivity of the surface $r_s = \langle r_s(\omega) \rangle_\omega$ (first column) and the deeper layer $r_1 = \langle r_1(\omega) \rangle_\omega$ (third column) averaged for photon energies between 45 eV and 65 eV. The images show a decrease in the *surface* reflectivity above the graphene. For samples with bilayer and trilayer films of graphene, this effect is pronounced. Recalling that the depositon process of the 200-nm Si layer and the handling was the same for all samples, we conclude that the decrease of signal from the surface above the graphene interfaces could be caused by an increased roughness of the surface. This, in turn, can be explained as the imprint of the graphene layer. Indeed, transferred graphene is known to exhibit a larger roughness compared to the surrounding substrate [29–31]. The increased roughness of the graphene sheet might be caused by residues of the PMMA transfer material or by mechanical defects [32]. A thorough analysis of the sample roughness can be done using a model-based approach which will be described in section 3.2 along with comparative atomic force microscopy measurements.

A *quantitative* comparison between different lateral positions and between the three samples is not directly possible because instabilities of the EUV source spectrum cause fluctuations in the retrieved reflectivity values. Since these instabilities affect the reflectivity signals of all interfaces at every lateral point, the fluctuations can be minimized by dividing the reflectivity of graphene r_1 (Fig. 2, third column) by the reflectivity of the surface r_S (first column). The result is shown in the fourth column of Fig. 2.

In Fig. 3, we compare the normalized reflectivity from the experiment with the results of a simple model. The experimental data points are mean values with the standard deviation as error bars. The reflectivity increases with the number of graphene layers, however not linearly. In contrast, the simple model shows a linear increase with the number of graphene layers. In
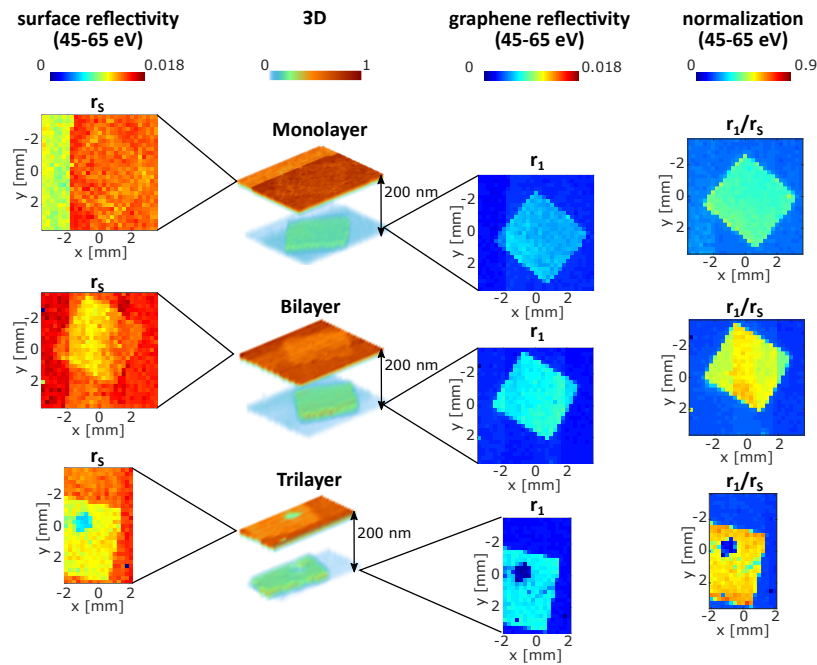
Fig. 2. Results of XCT measurements for graphene samples: monolayer (top), bilayer (middle) and trilayer (bottom). The reflectivity of individual interfaces (surface, first column and buried layers, third columns) are extracted from three-dimensional tomographic reconstructions of the sample (visualized in the second column). Each lateral position is obtained in an individual measurement. In the 3D renderings (second column), the color scale encodes the depth-resolved reflectivity, which is normalized to the overall maximum of all samples. For illustration purposes we rescaled the depth axis. The buried rectangular graphene flakes (4×4 mm) are resolved at 200 nm. The instability of the source causes regions of decreased signal (e.g. ML for $x < -2$ mm) and signal fluctuations between adjacent lateral points. Signal normalization (right column) reduces some of these effects. A dark area is still visible on the TL after normalization, meaning that it is caused by a sample defect and not by laser fluctuations.

addition, the model predicts a larger increase in reflectivity with increasing number of layers. Our model is based on the transfer matrix formalism [33] and dispersion data from [34]. We consider a smooth graphene layer between two layers of silicon. One possible explanation for the discrepancy between experiment and the simple model is the interface roughness reducing the reflectivity through scattering losses. This effect was already discussed above and also explains the lower surface reflectivity on top of the graphene. Another explanation is the presence of nanometer-thin oxide layer on both the substrate and the surface affecting the reflectivity. In the following, we present an extended model including interfacial roughnesses and oxide layers and show that both effects combined explain the observed discrepancies.

3.2. Model-based retrieval of interface parameters

The simple model that was used for Fig. 3(b) is extended by considering interface roughness and SiO_2 layers on the substrate and the sample surface. Since all three substrates are identical and the deposition process of the silicon layer was performed once for all samples, it can be assumed that the oxide thicknesses are the same for all samples. In contrast, as can be seen in Fig. 2 and as discussed above, the interface roughness of the graphene and the surface above
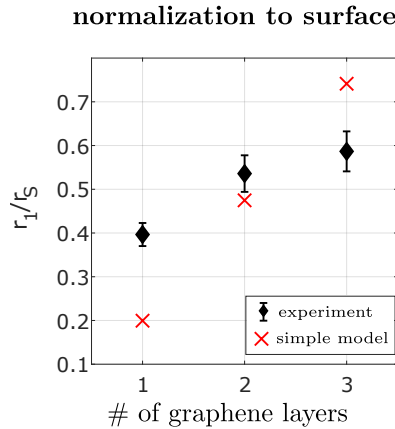
normalization to surface

Fig. 3. Comparison of experimentally obtained and modeled reflectivity of graphene r_1 normalized to the surface reflectivity r_S as a function of the number of graphene layers. The experimental data are presented as mean values with the standard deviation as error bars. The simple model predicts a linear increase of reflectivity with the number of layers.

does vary between samples. In total, for the three samples under consideration, this results in 8 independent parameters, the roughness at the surface (σ_{ML}^S, σ_{BL}^S, and σ_{TL}^S), the roughness of the graphene layer (σ_{ML}^1, σ_{BL}^1, and σ_{TL}^1), and the thicknesses of the native oxide layers on the surface d_S and on the substrate d_1. Each of these parameters can be linked to a measured reflectivity as described in the following.

Since XCT is a laterally resolving technique, several measurement points with partly redundant, partly entangled information are available. This provides sufficient conditions to determine the model parameters. We defined two lateral regions of interest (ROI) on the sample. One is the part of the sample with deposited graphene (ROI$_{gra}$) and the other (ROI$_{sub}$) is the rest of the sample around it. By averaging the XCT signal from the ROI's for each sample we extract 8 reflectivity values. Again, the reflectivities in ROI$_{sub}$ are the same for all three samples since they are manufactured in the same way. These reflectivities are measures of the thickness of the SiO$_2$ layers. The reflectivities of the graphene layer and the surface of the capping layer above it are measured for each of the three samples (6 values) and depend on the respective roughness of these interfaces. In summary, 8 experimental reflectivities are measured, which can be directly linked to the 8 unknown parameters (roughnesses, oxide thicknesses) of the model.

The fluctuations of the source spectrum discussed in section 3.1 impede a direct reconstruction of the model parameters. Again, we consider *ratios* of these reflectivities for the reconstruction. This minimizes the influence of fluctuations of the EUV source. In total $N = 10$ experimental ratios η can be extracted by normalization of the buried interface to the surface and by normalization of the reflectivity in (ROI$_{gra}$) to the surrounding (ROI$_{sub}$). These ratios can be used for subsequent fitting of the 8 model parameters and will be described in the following.

In Fig. 4, the two regions of interest and the ratios are shown for all samples. The formation of ratios is depicted by arrows indicating the corresponding division. The substrate reflectivity pointwise normalized to the surface reflectivity and subsequently averaged over ROI$_{sub}$ is denoted by

$$\eta_1 = \left\langle \frac{r_1^{ROI_{sub}}}{r_S^{ROI_{sub}}} \right\rangle_{x,y,ML,BL,TL} , \qquad (3)$$
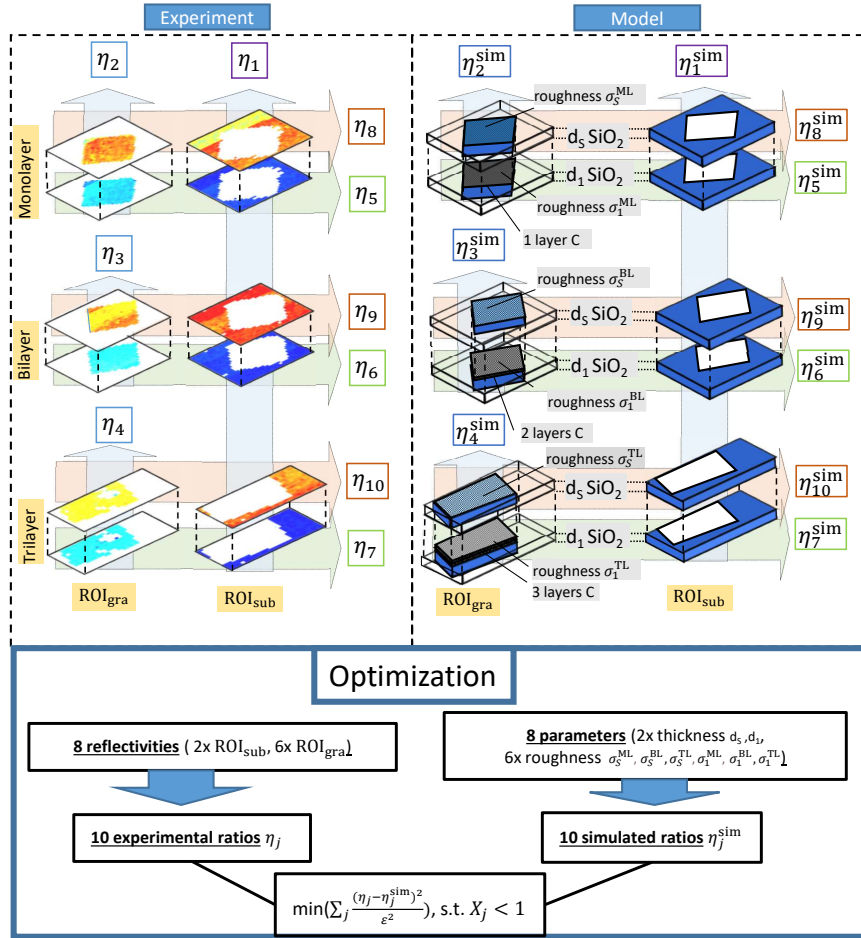
Fig. 4. Illustration of calculation of experimental and model ratios: We define two region of interest for each sample: area of graphene deposition (ROI_{gra}) and everything around (ROI_{sub}). From the experimental (left) and model (right) data we extract 10 coefficients as shown in Eq. (3)–6. See text for further details. The simulated and experimental ratios η_j and η_j^{sim} and the standard deviation of the experimental ratios ε_i are used to calculate the least-square error X_j^2, which is minimized ($\min\left[\sum_j X_j^2\right]$, s.t. $X_j^2 < 1$) to obtain the set of parameters (roughness and oxide thickness) of the best fit.

where $\langle \ldots \rangle_{x,y}$ indicates the lateral average over ROI_{sub}. As already explained, this normalized substrate reflectivity should be equal for all three samples and the average of the three measurements is used for η_1, indicated by the additional indices ML, BL, and TL in Eq. (3).

Three additional ratios

$$\eta_{2/3/4} = \left\langle \frac{r_1^{ROI_{gra}}}{r_S^{ROI_{gra}}} \right\rangle_{x,y}^{ML/BL/TL} . \tag{4}$$

are provided by the pointwise normalization of the graphene reflectivity to the surface reflectivity in ROI_{gra} for each of the three samples. The increase in reflectivity of the buried layer due to the

graphene in ROI_{gra} compared to the surrounding ROI_{sub} is described by

$$\eta_{5/6/7} = \left(\frac{\left\langle r_1^{\text{ROI}_{\text{gra}}} \right\rangle_{x,y}}{\left\langle r_1^{\text{ROI}_{\text{sub}}} \right\rangle_{x,y}} \right)^{\text{ML/BL/TL}}. \tag{5}$$

for each sample. Similarly,

$$\eta_{8/9/10} = \left(\frac{\left\langle r_S^{\text{ROI}_{\text{gra}}} \right\rangle_{x,y}}{\left\langle r_S^{\text{ROI}_{\text{sub}}} \right\rangle_{x,y}} \right)^{\text{ML/BL/TL}}. \tag{6}$$

describe the decrease in reflectivity (due to roughness) on the surface of the sample in ROI_{gra} above the deposited graphene compared to the surrounding area ROI_{sub}. These ratios η_{5-10} do not correct for the point-to-point fluctuations of the source spectrum but rather for variations of the source spectrum between the different samples.

The oxide thickness and interface roughness can now be obtained by minimizing the weighted least-square error

$$X^2 = \sum_{i=1}^{10} X_i^2 = \sum_{i=1}^{10} \left(\frac{\eta_i - \eta_i^{\text{sim}}}{\varepsilon_i} \right)^2 \tag{7}$$

between the experimental data η_i and the results of an extended model η_i^{sim}, considering the standard deviation of the experimental data, ε_i. Here, a grid with a discretization of 0.2 nm is used for each parameter. In addition, the condition $X_i^2 < 1$ is applied, meaning that for each individual coefficient, the modeled ratio is enforced to be within the standard deviation of the experiment.

The extended model is also based on the transfer matrix formalism [33]. As already pointed out, we now consider the thickness of the oxide layers and the roughnesses of the graphene and the surface above. For a multilayer systems, the latter is typically modeled by modifying the reflectivities of the interfaces with a Nevot-Croce factor [35]. However, this approach is not applicable if the roughness is larger than the layer thickness. For this reason, we use a slice method, which is numerically more complex but produces more accurate results [36,37]. In this method, the rough interface is modeled as a continuous transition. The density ratio of the materials at the interface changes as the error function, which corresponds to a Gaussian roughness distribution [38]. For modeling, this transition layer is discretized into slices of 0.1 nm with constant density.

The experimental reflectivity ratios η_i are shown in Fig. 5 in comparison to the modeled data η_i^{sim} for the minimal X^2. In Fig. 5(a) the ratios $\eta_{2,3,4}$, of the graphene normalized to the surface are shown in comparison to the extended model and the simple model from Fig. 3(b). The inclusion of interface roughness and oxide thickness yields an improved agreement of the experimental data and the extended model in comparison to the simple model from section 3.1.

In addition to this normalization to the surface, normalization was also performed within the different layers of the sample, η_{5-10}. This is shown in Fig. 5. The normalization of the graphene interface to the surrounding $\eta_{5,6,7}$ is shown as squares. The reflectivity is increased by a factor of 2 for the ML compared to the surrounding substrate ($\eta_5 \approx 2$) and even more for BL and TL ($\eta_{6,7} > 2$). The reflectivity of the surface above the graphene is identical to the surrounding for a ML of deposited graphene ($\eta_8 \approx 1$, diamonds) and decreases for BL and TL ($\eta_{9,10} < 1$). These experimental findings can be reproduced by the extended model as can be seen from the modeled ratios η_{5-7}^{sim} (blue) and η_{8-10}^{sim} (red).

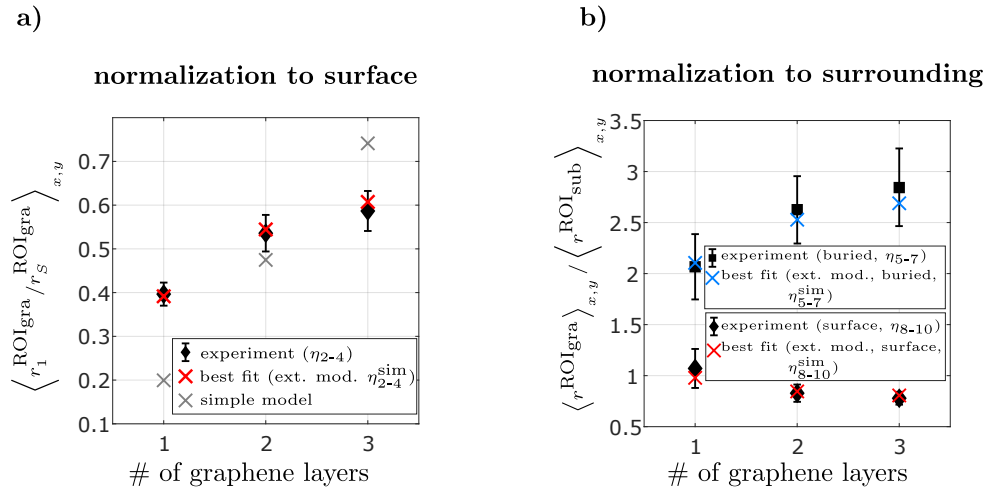a)   b)

Fig. 5. Comparison of the experimental ratios η with the model: a) Averaged values for the pointwise normalized reflectivity of the embedded graphene layer. The coefficients η which minimize the error X_i^2 are shown for comparison (crosses). The roughness and oxide thickness parameters used to calculate the ratios are summarized in Table 1. b) The normalization of the region ROI_{gra} with respect to the surrounding region ROI_{sub} is displayed for the surface (buried interface) as diamonds (squares). The corresponding results of the best fit model are shown in blue (red).

The sample parameters obtained by the modeling approach are shown in Table 1. The roughness increases with the number of graphene layers for the graphene interface itself ($\sigma_1^{ML} < \sigma_1^{BL} < \sigma_1^{TL}$) and the surface above ($\sigma_S^{ML} < \sigma_S^{BL} < \sigma_S^{TL}$). This can be explained by the deposition process: Each layer is transferred individually. This leads to an accumulation of transfer residue and fragmentations [39,40] and therefore to an increase in roughness. Note that for all samples the roughness is lower for the surface compared to the graphene interface. This can be explained by smoothing during the deposition.

Table 1. Parameters for roughness and oxide thickness from optimization using the extended model. In the last column, the values extracted from the AFM images shown in Fig. 6 are presented.

Parameter	XCT fit [nm]	XCT confidence interval [nm]	AFM[a] value [nm]
d_S	1.9	1.7-2.1	-
d_1	0.7	0.5-0.9	-
σ_S^{ML}	0.2	0.0-0.4	0.7
σ_1^{ML}	2.2	1.3-3.4	0.9[b]
σ_S^{BL}	1.6	0.4-2.4	1.4
σ_1^{BL}	3	2.8-7.6	1.2[b]
σ_S^{TL}	2.2	1.6-2.4	2.2
σ_1^{TL}	3.8	2.4-6	3.4[b]

[a]AFM values were obtained for a field of view of $8\,\mu m \times 8\,\mu m$, whereas XCT was averaged over several milimeters. Values where XCT and AFM match are marked olive, values were XCT and AFM measurements do not agree are shown in red. XCT and AFM measurements quantitatively agree in 50% of the cases.

[b]For the buried interface, AFM measurements had to be performed on additional uncoated samples from the same manufacturer.

To estimate the accuracy of our modeling for each parameter individually, each parameter was varied until the weighted sum $X^2 = \frac{1}{10} \sum_{i=1}^{10} X_i^2$ exceeded $X^2 = 1$ [41] or any X_i^2 exceeded $X_i^2 = 1$. The second condition was added since a multi-dimensional minimization process was used (see Fig. 4). Accordingly upper and lower bounds for each parameter were obtained.

To validate the findings of the XCT measurement and the extended model, we have characterized the surface topology by atomic force microscopy (AFM) measurements. The results are shown in Fig. 6. AFM measurements were performed on two sets of samples. Since AFM is only surface sensitive, only the surface of the samples that were imaged using XCT could be directly investigated. Therefore, the second set of samples was prepared without the deposition of the additional silicon layer and also measured with AFM. Based on the AFM measurements we conclude that the amount of the PMMA residuals and mechanical defects increases with the graphene thickness. For a quantitative comparison of the AFM results to XCT, the contribution of PMMA residual and mechanical defects to the roughness needs to be treated differently. The mechanical defects cause a lateral fluctuation of the z-position of the interface between silicon and carbon, which is described by the model. However, the roughness model does not incorporate the presence of PMMA grains at the interface. Additionally, these grains are much larger than the mechanical defects and lead to a strongly non-Gaussian roughness profile [42]. These grains are highlighted in Fig. 6 and excluded from statistics summarized in the last column of Table 1.
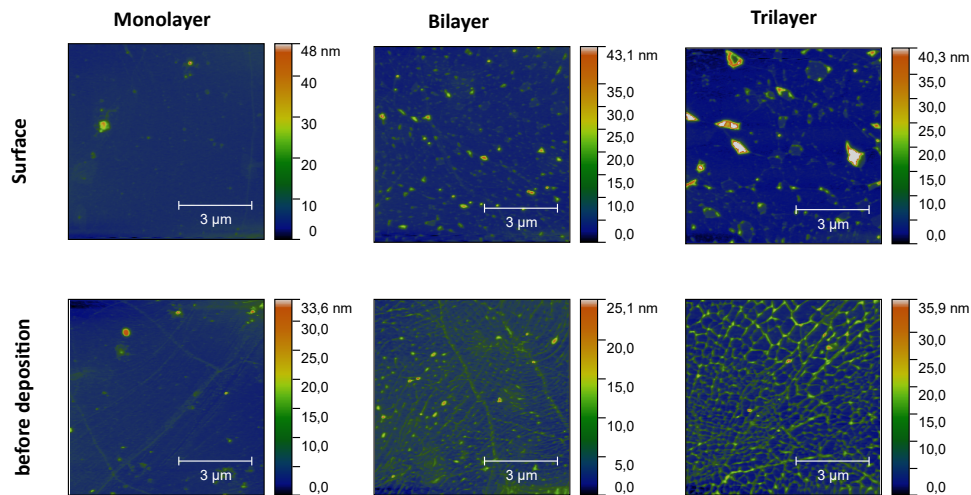

Fig. 6. Atomic force microscopy (AFM) images of the surface of the samples and the second set of samples without the 200 nm capping layer. As can also be seen in the XCT measurement, the roughness of both interfaces increases with the increasing number of layers. This is caused by the deposition process, where each layer is transferred individually. Two factors contribute to the roughness: Circular features visible in the AFM are residual PMMA from the transfer process. Additional roughness is caused by folding and breakage of the graphene flakes. The roughness model in XCT only includes the mechanical defects. For this reason, the masked areas (red) of large grains are neglected in the roughness analysis of the AFM data.

The AFM results, clearly confirm our observation that the surface roughness above the graphene increases for the BL and TL sample. Additionally, they confirm that the roughness on the surface is lower than on the graphene below, with the exception of the BL sample. However, the roughness of the graphene layer of the ML and BL sample and the surface layer of ML sample measured in the AFM is lower than the one estimated with XCT. The difference in roughness of the graphene layer are an indication to damages caused by the sputtering process. The AFM

images of the graphene on the substrate were taken without the deposition of the capping Si layer. In contrast, XCT investigates the sample after the deposition, including all changes to the interface that might occur during the deposition process. In addition, the small field of view of the AFM measurements ($8 \times 8 \ \mu$m) compared to the XCT ($50 \ \mu$m focal spot size) can also contribute to the deviation in measured roughness.

4. Discussion

We present results on the non-invasive and non-destructive investigation of graphene layers encapsulated in a Si matrix. XCT has been used to simultaneously characterize different graphene layers and the thickness and surface of the 200 nm thick capping layer of amorphous silicon. 3D tomographic images show that the reflectivity is enhanced in the area where the graphene layer is deposited. To investigate areas of 25 mm^2, a lateral scanning width of 250 μm stepsize was chosenThe EUV focal spot has a diameter of $\sim 50 \ \mu$m. The depth resolution is about $\delta_z = 27$ nm.

We have shown that XCT is able to differentiate between monolayers, bilayers, and trilayers of graphene buried under a Si layer by measuring an increasing reflectivity with the number of layers. Modeled data was optimized to the experimental data and, in result, the roughness of the graphene interface and the thickness of the native silicon oxide layers were obtained. Our investigation shows that the roughness of the graphene layers increases with the number of graphene layers. This is a drawback of the multiple transfer process of single graphene monolayers. Large graphene flakes fold and break during the transfer process, and PMMA residuals accumulate on the sample. This finding was confirmed by AFM measurements, which identify both PMMA residuals on the graphene and mechanical defects.

In addition to the characterization of the buried graphene layer, the size and quality of the encapsulating material was obtained. We show that the roughness of the graphene is connected to an increased roughness on the surface of the capping layer above the graphene. We emphasize that the thickness of the capping layer and the lateral position of the graphene as well as the reflectivities of both are measured directly without a model-based reconstruction. Moreover, by introducing an extended model, we are able to infer additional information such as the thickness of the native oxide layers and the interface roughness.

The stability of our measurement is mainly limited by the fluctuations of the EUV source. Due to the lateral and axial resolution provided by XCT, it is possible to minimize this effect in the model-based calculations by only considering ratios of measured reflectivities. Nevertheless, the roughness measured with XCT deviates from the AFM measurements for some interfaces in the mono- and bilayer sample. For the graphene interface XCT measures the roughness after the depostion of the capping Si layer and is therefore sensitive to any damages caused by the sputtering process. Since AFM is not a depth-resolving technique, the AFM measurements of the buried interface had to be performed on a second set of samples without the capping layer. In addition, in XCT the roughness is averaged over a larger area compared to the smaller field of view of the AFM.

The imaging depth of XCT is not limited to 200 nm which was used in this work. The used spectrometer enables the measurement of axial distances of up to $\sim 2 \ \mu$m [24]. In addition, more complex samples of multiple layers were already imaged with XCT [26].

In comparison to other techniques for cross-sectional imaging (e.g. cross-sectional TEM), XCT probes the cross-sectional structure of a layered sample by non-destructive and contact-free measurements. XCT at higher photon energies would allow to investigate graphene layers buried under other materials [18,43].

3D imaging of graphene with XCT can be regarded as an important step towards non-destructive and non-contact characterization of gaphene based electronics [44] such as sensors, transistors, etc. buried in protective matrices. XCT can also be used to image samples with a higher axial complexity than presented in this work [19]. The technology could be integrated in a

production line, giving instant feedback on the quality of graphene. The technique can also measure buried and encapsulated conducting layers, which provides essential information on the impact of intermediate process steps on the electrical characteristics during device fabrication. We anticipate that XCT will find applications in the non-invasive and non-contact inspection of graphene-based sensors and devices.

Disclosures. The authors declare that there are no conflicts of interest related to this article.

Data availability. Data underlying the results presented in this paper are not publicly available at this time but may be obtained from the authors upon reasonable request.

References

1. K. S. Novoselov, A. K. Geim, S. V. Morozov, D. Jiang, Y. Zhang, S. V. Dubonos, I. V. Grigorieva, and A. A. Firsov, "Electric field effect in atomically thin carbon films," Science **306**(5696), 666–669 (2004).
2. A. H. Castro Neto, F. Guinea, N. M. R. Peres, K. S. Novoselov, and A. K. Geim, "The electronic properties of graphene," Rev. Mod. Phys. **81**(1), 109–162 (2009).
3. S. Das Sarma, S. Adam, E. H. Hwang, and E. Rossi, "Electronic transport in two-dimensional graphene," Rev. Mod. Phys. **83**(2), 407–470 (2011).
4. Y. Huang, J. Liang, and Y. Chen, "An overview of the applications of graphene-based materials in supercapacitors," Small **8**(12), 1805–1834 (2012).
5. C. Chung, Y.-K. Kim, D. Shin, S.-R. Ryoo, B. H. Hong, and D.-H. Min, "Biomedical applications of graphene and graphene oxide," Acc. Chem. Res. **46**(10), 2211–2224 (2013).
6. D. N. Basov, M. M. Fogler, A. Lanzara, F. Wang, and Y. Zhang, "Colloquium: Graphene spectroscopy," Rev. Mod. Phys. **86**(3), 959–994 (2014).
7. A. C. Ferrari, J. C. Meyer, V. Scardaci, C. Casiraghi, M. Lazzeri, F. Mauri, S. Piscanec, D. Jiang, K. S. Novoselov, S. Roth, and A. K. Geim, "Raman spectrum of graphene and graphene layers," Phys. Rev. Lett. **97**(18), 187401 (2006).
8. A. C. Ferrari and D. M. Basko, "Raman spectroscopy as a versatile tool for studying the properties of graphene," Nat. Nanotechnol. **8**(4), 235–246 (2013).
9. M. Telychko, P. Mutombo, P. Merino, P. Hapala, M. Ondráček, F. C. Bocquet, J. Sforzini, O. Stetsovych, M. Vondráček, P. Jelínek, and M. Švec, "Electronic and chemical properties of donor, acceptor centers in graphene," ACS Nano **9**(9), 9180–9187 (2015).
10. R. S. Pantelic, J. C. Meyer, U. Kaiser, and H. Stahlberg, "The application of graphene as a sample support in transmission electron microscopy," Solid State Commun. **152**(15), 1375–1382 (2012).
11. P. Merino, M. Švec, A. L. Pinardi, G. Otero, and J. A. Martín-Gago, "Strain-driven moiré superstructures of epitaxial graphene on transition metal surfaces," ACS Nano **5**(7), 5627–5634 (2011).
12. L. Chen, Y. Hernandez, X. Feng, and K. Müllen, "From nanographene and graphene nanoribbons to graphene sheets: Chemical synthesis," Angew. Chem. Int. Ed. **51**(31), 7640–7654 (2012).
13. Y. Yu, Z. Li, W. Wang, X. Guo, J. Jiang, H. Nan, and Z. Ni, "Investigation of multilayer domains in large-scale CVD monolayer graphene by optical imaging," J. Semicond. **38**(3), 033003 (2017).
14. I. H. Abidi, L.-T. Weng, C. P. J. Wong, A. Tyagi, L. Gan, Y. Ding, M. Li, Z. Gao, R. Xue, M. D. Hossain, M. Zhuang, X. Ou, and Z. Luo, "New approach to unveiling individual atomic layers of 2d materials and their heterostructures," Chem. Mater. **30**(5), 1718–1728 (2018).
15. C. Backes, A. M. Abdelkader, and C. Alonso, *et al.*, "Production and processing of graphene and related materials," 2D Mater. **7**(2), 022001 (2020).
16. S. Yoo and Q.-H. Park, "Spectroscopic ellipsometry for low-dimensional materials and heterostructures," Nanophotonics **11**(12), 2811–2825 (2022).
17. E. Simsek and B. Mukherjee, "Visibility of atomically-thin layered materials buried in silicon dioxide," Nanotechnology **26**(45), 455701 (2015).
18. S. Fuchs, C. Rödel, A. Blinne, U. Zastrau, M. Wünsche, V. Hilbert, L. Glaser, J. Viefhaus, E. Frumker, P. Corkum, E. Förster, and G. G. Paulus, "Nanometer resolution optical coherence tomography using broad bandwidth XUV and soft x-ray radiation," Sci. Rep. **6**(1), 20658 (2016).
19. S. Fuchs, M. Wünsche, J. Nathanael, J. J. Abel, C. Rödel, J. Biedermann, J. Reinhard, U. Hübner, and G. G. Paulus, "Optical coherence tomography with nanoscale axial resolution using a laser-driven high-harmonic source," Optica **4**(8), 903–906 (2017).

20. S. Skruszewicz, S. Fuchs, J. J. Abel, J. Nathanael, J. Reinhard, C. Rödel, F. Wiesner, M. Wünsche, P. Wachulak, A. Bartnik, K. Janulewicz, H. Fiedorowicz, and G. G. Paulus, "Coherence tomography with broad bandwidth extreme ultraviolet and soft X-ray radiation," Appl. Phys. B **127**(4), 55 (2021).

21. J. Nathanael, M. Wünsche, S. Fuchs, T. Weber, J. J. Abel, J. Reinhard, F. Wiesner, U. Hübner, S. J. Skruszewicz, G. G. Paulus, and C. Rödel, "Laboratory setup for extreme ultraviolet coherence tomography driven by a high-harmonic source," Rev. Sci. Instrum. **90**(11), 113702 (2019).

22. M. Ferray, A. L'Huillier, X. F. Li, L. A. Lompre, G. Mainfray, and C. Manus, "Multiple-harmonic conversion of 1064 nm radiation in rare gases," J. Phys. B: At., Mol. Opt. Phys. **21**(3), L31–L35 (1988).

23. M. Wünsche, S. Fuchs, S. Aull, J. Nathanael, M. Möller, C. Rödel, and G. G. Paulus, "Quasi-supercontinuum source in the extreme ultraviolet using multiple frequency combs from high-harmonic generation," Opt. Express **25**(6), 6936–6944 (2017).

24. M. Wünsche, S. Fuchs, T. Weber, J. Nathanael, J. J. Abel, J. Reinhard, F. Wiesner, U. Hübner, S. J. Skruszewicz, G. G. Paulus, and C. Rödel, "A high resolution extreme ultraviolet spectrometer system optimized for harmonic spectroscopy and XUV beam analysis," Rev. Sci. Instrum. **90**(2), 023108 (2019).

25. S. Fuchs, A. Blinne, C. Rödel, U. Zastrau, V. Hilbert, M. Wünsche, J. Bierbach, E. Frumker, E. Förster, and G. G. Paulus, "Optical coherence tomography using broad-bandwidth xuv and soft x-ray radiation," Appl. Phys. B: Lasers Opt. **106**(4), 789–795 (2012).

26. F. Wiesner, F. Wiesner, M. Wünsche, M. Wünsche, J. Reinhard, J. Reinhard, J. J. Abel, J. Nathanael, J. Nathanael, S. Skruszewicz, C. Rödel, S. Yulin, A. Gawlik, G. Schmidl, U. Hübner, J. Plentz, G. G. Paulus, G. G. Paulus, S. Fuchs, and S. Fuchs, "Material-specific imaging of nanolayers using extreme ultraviolet coherence tomography," Optica **8**(2), 230–238 (2021).

27. Graphenea, https://www.graphenea.com/.

28. Z. H. Ni, H. M. Wang, J. Kasim, H. M. Fan, T. Yu, Y. H. Wu, Y. P. Feng, and Z. X. Shen, "Graphene thickness determination using reflection and contrast spectroscopy," Nano Lett. **7**(9), 2758–2763 (2007).

29. Y.-P. Wang, H. Zhou, L. Zhou, R. L. Headrick, A. T. Macrander, and A. S. Özcan, "Interface roughness evolution in sputtered w si 2/ si multilayers," J. Appl. Phys. **101**(2), 023503 (2007).

30. A. Ulyanenkov, R. Matsuo, K. Omote, K. Inaba, J. Harada, M. Ishino, M. Nishii, and O. Yoda, "X-ray scattering study of interfacial roughness correlation in Mo/Si multilayers fabricated by ion beam sputtering," J. Appl. Phys. **87**(10), 7255–7260 (2000).

31. M. Putero-Vuaroqueaux, H. Faik, and B. Vidal, "A comparative study of the interfacial roughness correlation and propagation in mo/si multilayers deposited using rf-magnetron sputtering on silicon, ule and zerodur substrates," J. Phys.: Condens. Matter **14**(39), 8955–8968 (2002).

32. G. B. Barin, Y. Song, I. de Fátima Gimenez, A. G. Souza Filho, L. S. Barreto, and J. Kong, "Optimized graphene transfer: Influence of polymethylmethacrylate (pmma) layer concentration and baking time on graphene final performance," Carbon **84**, 82–90 (2015).

33. B. E. Saleh and M. C. Teich, *Fundamentals of photonics* (John Wiley & sons, 2019).

34. B. L. Henke, E. M. Gullikson, and J. C. Davis, "X-ray interactions: photoabsorption, scattering, transmission and reflection E= 50-30, 000 eV, Z= 1-92," At. Data Nucl. Data Tables **54**(2), 181–342 (1993).

35. L. Névot and P. Croce, "Caractérisation des surfaces par réflexion rasante de rayons X. Application à l'étude du polissage de quelques verres silicates," Rev. Phys. Appl. **15**(3), 761–779 (1980).

36. M. Tolan, *X-ray scattering from soft-matter thin films: materials science and basic research*, vol. 148 (Springer, 1999).

37. D. De Boer, "Influence of the roughness profile on the specular reflectivity of x rays and neutrons," Phys. Rev. B **49**(9), 5817–5820 (1994).

38. K. Stoev and K. Sakurai, "Recent theoretical models in grazing incidence x-ray reflectometry," The Rigaku Journal **14**, 22–37 (1997).

39. J. Kang, D. Shin, S. Bae, and B. H. Hong, "Graphene transfer: key for applications," Nanoscale **4**(18), 5527–5537 (2012).

40. Y. Wang, S. W. Tong, X. F. Xu, B. Özyilmaz, and K. P. Loh, "Interface engineering of layer-by-layer stacked graphene anodes for high-performance organic solar cells," Adv. Mater. **23**(13), 1514–1518 (2011).

41. M. Tanksalvala, C. L. Porter, and Y. Esashi, *et al.*, "Nondestructive, high-resolution, chemically specific 3D nanostructure characterization using phase-sensitive EUV imaging reflectometry," Sci. Adv. **7**(5), eabd9667 (2021).

42. V. Mironov, O. Udalov, B. Gribkov, and A. Fraerman, "Comparative x-ray reflectometry and atomic force microscopy of surfaces with non-gaussian roughness," J. Appl. Phys. **104**(6), 064301 (2008).

43. P. Wachulak, A. Bartnik, and H. Fiedorowicz, "Optical coherence tomography (OCT) with 2 nm axial resolution using a compact laser plasma soft x-ray source," Sci. Rep. **8**(1), 8494 (2018).

44. M. Sang, J. Shin, K. Kim, and K. J. Yu, "Electronic and thermal properties of graphene and recent advances in graphene based electronics applications," Nanomaterials **9**(3), 374 (2019).